Journal of Materials Chemistry C

ROYAL SOCIETY OF CHEMISTRY

PAPER

View Article Online
View Journal | View Issue

Cite this: J. Mater. Chem. C, 2022, 10, 2608

Molecular spinterface in F_4TCNQ-doped polymer spin valves†‡

Dongxue Yu,[a] Shuaishuai Ding, *[a] Jing Li,[a] Wenbo Mi, [b] Yuan Tian*[c] and Wenping Hu*[ad]

Received 8th September 2021,
Accepted 4th October 2021

DOI: 10.1039/d1tc04259a

rsc.li/materials-c

The molecular spinterface is an ideal platform to realize multistate storage in organic spin valve (OSV) devices. However, as an effective strategy to enhance the conductivity and modify the spinterface, molecular doping has rarely been reported in vertical OSV devices, and the effect of artificial doping induced spinterface is not clear yet. Herein, we fabricated a F_4TCNQ-doped polymer spin valve with a stacking structure of $La_{2/3}Sr_{1/3}MO_3$ (LSMO)/poly(3-hexylthiophene-2,5-diyl) (P3HT)/tetrafluoro-tetracyanoquinodimethane (F_4TCNQ)/Co/Au, and found a significant improvement in conductivity and the magnetoresistance (MR) ratio. According to the characterization of interfacial states and investigation of half spin valves, it was determined that F_4TCNQ was doped in the form of free radicals and created a spin-dependent hybrid interfacial state (SDHIS). Such a SDHIS can exhibit an extra interface magnetoresistance (IMR) effect imposed on the standard giant magnetoresistance (GMR) effect. This interfacial doping strategy shows great potential for application in future multistate molecular spintronic devices and provides a new insight into the mechanism of radical-induced molecular spinterface.

1. Introduction

In 1988, German scientist Peter Grünberg and French scientist Albert Fert independently discovered the giant magnetoresistance effect (GMR) and shared the Nobel Prize in Physics in 2007.[1] Since then, GMR has successfully opened a new door to modern information storage with spintronics. Spin is one of the basic properties of electrons, as well as the basis of chemical properties such as molecular magnetism and free radical reactions. With further research and wide application of spintronics, traditional inorganic spin valves suffer from major limitations such as high cost, rigid temperature treatment and lattice matching requirements.[2] In comparison, organic materials with good solution processability, low cost, excellent flexibility and diverse chemical modifications can make up for the above deficiencies.[3–6] Particularly, due to the small atomic number of constituent elements, organic materials exhibit weak hyperfine interactions and long spin relaxation times, and are considered as very promising materials for spin transport applications.[7–11] In 2004, Xiong *et al.* reported the first vertical organic spin valve (OSV) device using the organic semiconductor Alq_3 as the intermediate layer sandwiched between ferromagnetic (FM) LSMO and cobalt (Co), opening the new era of molecular spintronics.[12] From then on considerable progress has been made in both theoretical investigations and integrated multifunctional devices on the foundation of the OSV prototype.[13–17]

The organic semiconductor materials adopted in OSVs mainly include small molecules and polymers.[18–20] As for the spin transport in π-conjugated polymers, their spin diffusion length (λ_s) will be limited by the relatively low mobility (μ) of the localized polarons which is governed by the thermally activated hopping mechanism, considering the relationship of $\lambda_s = \sqrt{\mu k_B T \tau / e}$.[21,22] Moreover, the large resistivity of the organic intermediate layer is also a bottleneck for spin injection from most FM electrodes due to the famous conductivity mismatch problem.[2,23] To solve these problems, replacing FM electrodes with optimized spin injection efficiency is effective but not the only option.[24–26] In contrast, based on the huge influence of the spinterface on the device performance, modification of the spinterface may provide a new insight into the spin injection enhanced performance.[27,28] Many scientists have found that the change of the spinterface can greatly influence the performance of the device by enhancing/inversing the magnetoresistance (MR) response, increasing the spin injection efficiency and so on.[29–33] In addition, recent studies have shown that molecular doping can significantly improve the chemical tunability advantage of organic

[a] Tianjin Key Laboratory of Molecular Optoelectronic Sciences, Department of Chemistry, School of Sciences, Tianjin University, Tianjin 300072, China. E-mail: dingshuaishuai@tju.edu.cn, huwp@tju.edu.cn
[b] Tianjin Key Laboratory of Low Dimensional Materials Physics and Preparation Technology, School of Science, Tianjin University, Tianjin 300354, China
[c] School of Physics & Electronics, Hunan University, Hunan 410082, China. E-mail: ytian@hnu.edu.cn
[d] Joint School of National University of Singapore and Tianjin University, International Campus of Tianjin University, Binhai New City, Fuzhou 350207, China

† Dedicated to Professor Daoben Zhu on the occasion of his 80th birthday.
‡ Electronic supplementary information (ESI) available. See DOI: 10.1039/d1tc04259a

materials and further boost the spin diffusion length by increasing the conductivity *via* a transverse spin pumping approach.[34–38] However, such an interfacial doping strategy has rarely been proved in vertical spin valve devices, and the hybrid spin-polarized states formed by both the dopant and FM electrode still remain unclear. Therefore, it is necessary to establish a platform to investigate the doping induced spinterface in OSVs.

In this work, we constructed a π-conjugated polymer spin valve with a vertical structure of LSMO/P3HT/F_4TCNQ/Co/Au to explore the effect of F_4TCNQ doping on the spinterface. Here, we adopted a solution-sequential processing (SqP) method by doping a widely used p-type dopant, F_4TCNQ, on the polymer P3HT layer to optimize the spinterface and reduce the device resistance.[39] Compared with the undoped device, the conductivity and giant magnetoresistance (GMR) response of the doped LSMO/P3HT/F_4TCNQ/Co/Au showed a significant increase with an increase of the coercivity of the FM electrode Co. In order to further study the role of doping induced spinterface in performance optimization, the FM LSMO electrode was replaced by a non-FM ITO electrode. It was observed that doping not only adjusts the electron injection barrier but also changes the temperature-dependent device resistance. More importantly, we verified that the F_4TCNQ was doped in the form of radicals and served as an effective spin filter, which may be utilized to achieve multistate and even new-type spintronic devices. These findings will provide ideas for promoting the development of organic spin valves and optimizing the spinterface spontaneously.

2. Experimental section

2.1. Device fabrication

In this experiment, we prepared a polymer spin valve with a vertical structure of LSMO (100 nm)/P3HT (~40 nm)/F_4TCNQ/Co (15 nm)/Au (25 nm). The structure contains an effective overlapping junction area of 500 μm × 600 μm.

Fabrication of the bottom LSMO electrode. A 500 μm-wide LSMO FM electrode on a $SrTiO_3$ substrate was fabricated by direct current facing-target magnetron sputtering technology and was used as the bottom electrode.[30,40] It was cleaned with isopropanol, ultrasonicated using an ultrasonic cleaner for 10–20 s, and dried with N_2 stream, successively.

Preparation of the organic spacer. We used regioregular poly(3-hexylthiophene-2,5-diyl) (RR-P3HT) powder (stereoregularity ≥99%, molecular weight of number average from 27 000 to 45 000, TCI Chemicals) and 1,2-dichlorobenzene (≥99%, Acros Inc.) as the polymer intermediate layer and solvent, respectively. A P3HT solution with a concentration of 10 mg mL^{-1} was prepared. The solution was heated and stirred continuously on a heating stage at 70 °C for 30 min and filtered through a 0.22 μm organic phase syringe filter to obtain a uniform and clear solution. The P3HT layer was spin-coated at a rotating speed of 2000 rpm for 60 s and then annealed at 120 °C for 5 min. 2,3,5,6-Tetrafluoro-7,7,8,8-tetracyanoquinodimethane (F_4TCNQ, purified by sublimation, TCI Chemicals) and butyl acetate (colorless clear liquid, purity (GC) ≥99.0%, TCI Chemicals) were adopted as the dopant and solvent, respectively. The concentration of F_4TCNQ solution was 1 mg mL^{-1}. The F_4TCNQ solution was uniformly mixed by ultrasonication, the power was set as 40%, and the ultrasonic time was 2 min. The doping was carried out by means of spin coating as well. The spin speed was 6000 rpm with a spin time of 60 s. All spin-coating operations were completed in a clean room to avoid additional contamination.

Evaporation of the top Co electrode. The Co FM electrode and Au protecting layer were evaporated with a shadow mask in a thermal evaporation system in a glovebox. The base pressure was 1×10^{-6} torr. The evaporation rates of Co and Au were 0.1 Å s^{-1} and 0.3 Å s^{-1}, respectively. During the evaporation processes of Co and Au, we used a customized evaporation boat to reduce possible damage from thermal radiation.

Meanwhile, we also prepared a half spin valve device with a vertical structure of ITO/P3HT/F_4TCNQ/Co/Au for comparison. An ITO electrode was ultrasonically cleaned by isopropanol 3 times with a cleaning power of 40% and 5 minutes each time. Then the preparation of the P3HT organic layer, the process of spin-coated doping and the evaporation of the top Co electrode were the same as those mentioned above. It should be emphasized that the spin coating speed for P3HT was calibrated to maintain the same thickness as well.

2.2. Characterization

The surface morphology and layer thickness of the samples were characterized using an optical microscope (Eclipse Ci-POL, Nikon, Japan) and an atomic force microscope (AFM, Dimension Icon, Bruker) in tapping mode. An ultraviolet-visible-near infrared (UV-vis-NIR) spectrophotometer (UV-3600 Plus, Shimadzu) and a Fourier transform infrared (FT-IR) spectrometer (Vertex 70, Bruker) were used to characterize the effectiveness of doping. In the magnetic characterization, the coercivity of the Co electrode on top of various thin films was measured using the vibration sample magnetometer (VSM) module of a physical property measurement system (PPMS DynaCool, Quantum Design). Resistance and magnetoresistance (MR) as a function of temperature and input current were measured using the built-in DC-transport option of the PPMS with a motorized horizontal rotator module. The LSMO (Co) electrode was attached to *V*+ (*V*−) and *I*+ (*I*−) pin connector terminations with silver paste. It should be noted that a magnetic field was applied along the long side of the rectangular LSMO strip. The current–voltage (*I*–*V*) curve measurements were carried out using an external Keithley 2636B Dual-Channel System Source Meter Unit (SMU) interfaced to the PPMS, and the Co electrode was grounded during the measurement.

3. Results and discussion

3.1. MR response of the polymer spin valve

Firstly, we investigated the influence of doping on the MR of the OSV device. Fig. 1a shows a schematic diagram of the spin valve device structure of LSMO/P3HT/F_4TCNQ/Co/Au. A small

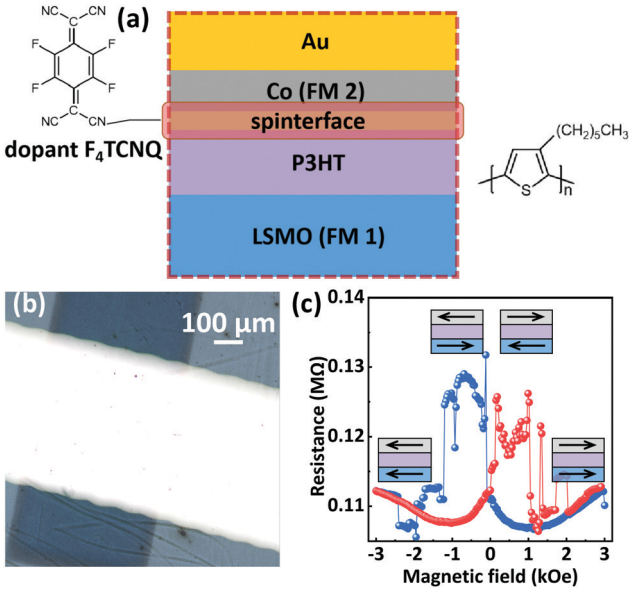

Fig. 1 (a) The structure diagram of the polymer spin valve with a vertically stacking device structure of LSMO (100 nm)/P3HT (~40 nm)/F_4TCNQ/Co (15 nm)/Au (25 nm). (b) Optical microscope image of the LSMO/P3HT/F_4TCNQ/Co/Au device. (c) Typical MR curve of the LSMO/P3HT/F_4TCNQ/Co/Au device at a temperature of T = 2 K and a current of I = 0.01 μA. Insets show the relative magnetization directions of LSMO (blue) and Co (grey) under various external magnetic fields, respectively.

organic molecule, F_4TCNQ, has an electron affinity (E_A) of 5.24 eV, which is a good electron-accepting dopant.[41] We used F_4TCNQ to dope the spin-coated P3HT thin film through the SqP approach.[39] Hole charge carriers and spin signals were injected from the LSMO electrode and transferred to the Co electrode through the F_4TCNQ-doped P3HT space layer, considering their relative energy level relationship (Fig. S1, ESI‡) and the direction of the input source.[12,30,42,43] Fig. 1b shows an optical microscope image after evaporation, and the effective junction area of the device is clearly defined as 500 μm × 600 μm. The granular aggregates induced by F_4TCNQ doping are shown in Fig. S2 (ESI‡).

Fig. 1c shows a typical magnetic response curve of the doped LSMO/P3HT/F_4TCNQ/Co/Au device and its corresponding working states. The blue (red) dotted line represents the real-time device resistance when the external magnetic field was sweeping from +3000 Oe (−3000 Oe) to −3000 Oe (+3000 Oe). Because the coercive forces of the bottom LSMO and top Co FM electrodes are different, the relative magnetization directions of the LSMO and Co electrodes can be adjusted by changing the value and direction of the applied magnetic field. If the magnetization directions of the LSMO and Co electrodes are in an anti-parallel alignment, it is difficult for the carriers to maintain the spin signals when entering the counter electrode due to spin-dependent scattering, resulting in a high resistance state. If their magnetization directions are parallel, the charge carriers will easily reach the Co electrode, leading to a low resistance state.[44,45] Thus, the control of the resistance states in a doped-P3HT spin valve device was realized, and the different stages are shown in Fig. 1c.

The MR ratio is one of the key parameters in the performance evaluation of the OSV devices. It is defined as MR = $(R_{AP} - R_P)/R_P$, where R_{AP} (R_P) is the device resistance in anti-parallel (parallel) magnetization alignment. At T = 2 K, the device exhibited a normal positive GMR response by taking the thickness of the doped P3HT thin film into account (Fig. S4f, ESI‡),[18] and the MR ratio was about 19%. Compared with the non-doped device of the same organic spacer thickness (Fig. S3, ESI‡), the GMR effect of the doped device has been significantly improved. Moreover, we found that the average resistance of the doped device decreased significantly from 10^7 Ω to 10^5 Ω.

Next, we investigate the evolution patterns on the MR curves of the F_4TCNQ-doped OSV devices in detail. In order to find the best temperature and current ranges to boost the signal response of the device, the measurements were carried out at 5 different temperatures and 4 different input currents. Fig. 2 shows the MR curve of the doped LSMO/P3HT/F_4TCNQ/Co/Au device at the same temperature of 5 K; the MR ratio of the device decreases as the applied current increases. At 0.01 μA, the MR is 16%, while it is reduced to only 11% at 0.05 μA. This could be explained by the shift of the relative Fermi level position of the separate layers in the device and consequently the variation of effective spin polarization when changing the bias current.[11] Fig. 3(a–c) show the MR curves of the same input current of 0.01 μA at different monitoring temperatures. Besides there was an obvious reduction of the MR ratio from 19% to 11% as the temperature was increased from 2 K to 20 K, and the switching field of the Co electrode also decreased, indicating decreases in both the coercivity and spin polarization ratio of FM electrodes. Fig. 3d presents the MR ratio of the doped device as a function of temperature and bias current. The MR ratio of the LSMO/P3HT/F_4TCNQ/Co/Au device

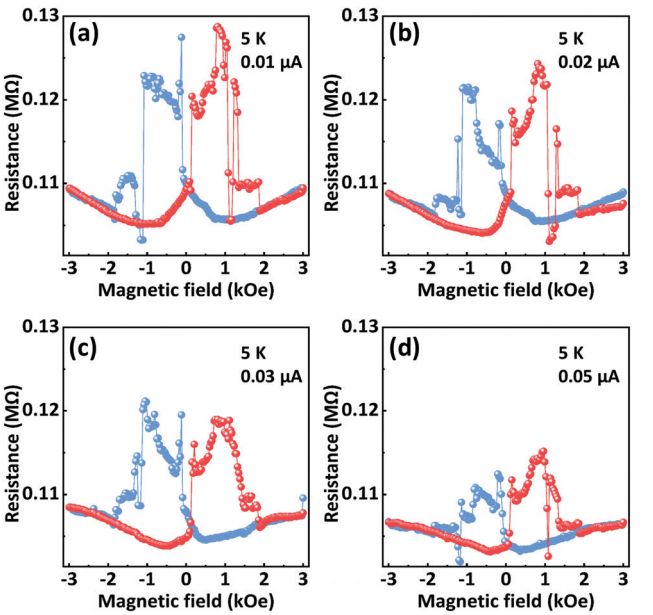

Fig. 2 The MR curves of the LSMO/P3HT/F_4TCNQ/Co/Au device as a function of input current at T = 5 K. The input current was set as (a) 0.01 μA, (b) 0.02 μA, (c) 0.03 μA, and (d) 0.05 μA, respectively.

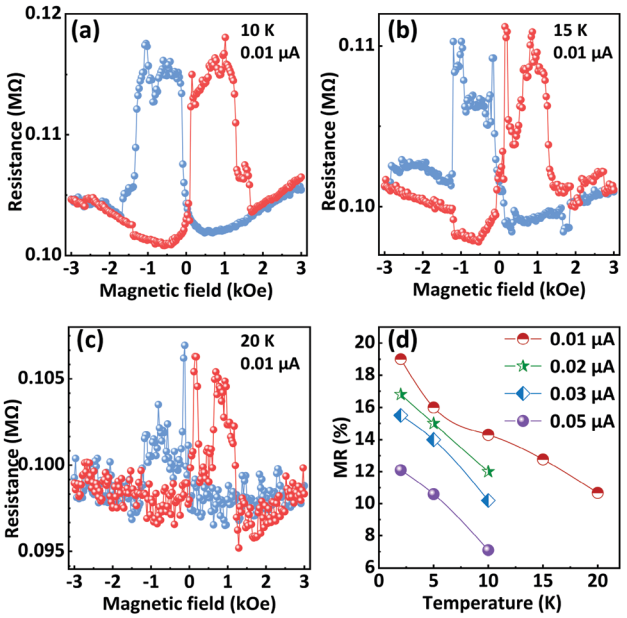

Fig. 3 The MR curves of the LSMO/P3HT/F_4TCNQ/Co/Au device when (a) T = 10 K, (b) T = 15 K, and (c) T = 20 K at a constant input current of 0.01 μA, respectively. (d) Bias current and temperature dependences of the MR ratio of the doped device.

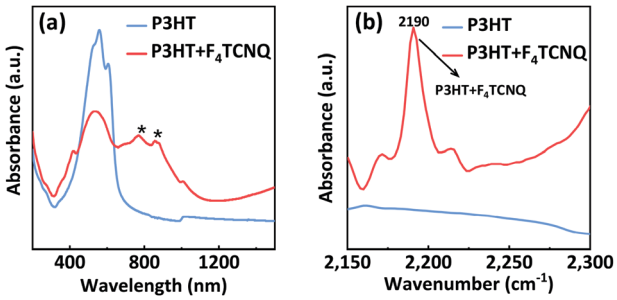

Fig. 4 (a) UV-vis spectra and (b) FT-IR spectra of the pristine P3HT and F_4TCNQ-doped thin films.

decreases with the increase of both temperature and current under all conditions, which is in good agreement with the characteristics of classic GMR transport.[46] As a result, the MR is the largest under the conditions of T = 2 K and I = 0.01 μA.

As for the line shape of MR curves, it seems that two repeatable resistance terraces appeared at around 1400 Oe and 1900 Oe for each dotted line in the entire input current range (Fig. 2), which was different from the reported OSV devices with only one platform in each sweeping direction.[25,40,47] We also found that the width of the resistance terrace varies as the temperature changes. Particularly, a jump discontinuity at around 300 Oe emerged at 15 K and even became dominant at 20 K. We speculate that the competitive factors of the magnetic response might be related to the F_4TCNQ-doping induced non-trivial spinterface, which will be demonstrated in the following part.

3.2. Characterization of the doping interface

In order to gain a better understanding of the mechanism of the improved MR effect and influence of the spinterface after doping, we need to carefully investigate the interfacial state and doping degree of the F_4TCNQ-doped P3HT thin film.

We firstly compared the surface morphology and film thickness before and after doping (Fig. S4, ESI‡). The surface roughness increased after doping, from R_q = 5.4 nm and R_a = 4.4 nm in Fig. S4a (ESI‡) to R_q = 7.1 nm and R_a = 5.7 nm in Fig. S4b (ESI‡). This can be explained by the fact that the residual F_4TCNQ aggregated islands formed high points on the surface of the P3HT thin film (Fig. S4b and c, ESI‡). The thickness of the organic space layer increased slightly after doping from 42 nm in Fig. S4d (ESI‡) to 44 nm in Fig. S4e (ESI‡). Therefore, it can be known that the doping has little effect on the thickness of the P3HT layer.

It is well known that the efficiency of molecular doping strongly depends on the doping method and concentration.[39,48] In previous studies, it has been reported that F_4TCNQ existed in the form of anions after doping.[49,50] In order to verify the doping mode of F_4TCNQ, we recorded the UV-vis and FT-IR spectra. In Fig. 4a, two new characteristic peaks at 768 nm and 860 nm appeared after doping, which represents the formation of a F_4TCNQ radical.[51] In the FT-IR spectra (Fig. 4b), new chemical bonds formed after doping at a wavenumber of 2190 cm^{-1}. In the neutral F_4TCNQ sample, C≡N stretching occurs at 2227 cm^{-1}. If F_4TCNQ is fully ionized to F_4TCNQ^-, C≡N will redshift from 33 cm^{-1} to 2194 cm^{-1}. The spectra of P3HT/F_4TCNQ in Fig. 4b showed a shift towards 2190 cm^{-1}, which is almost close to 2194 cm^{-1}, indicating complete ionization.[52] These results prove that the P3HT layer was effectively doped by F_4TCNQ through the SqP strategy.

Then we investigated the influence of doping on the interfacial magnetic properties. We characterized the coercivity change in the magnetization curves of the thermally evaporated Co electrode on three different surfaces, *i.e.*, on silicon oxide wafer, pristine P3HT thin film, and F_4TCNQ-doped P3HT thin film (Fig. 5). Their corresponding average coercivity values were 110 Oe, 540 Oe, and 890 Oe at T = 2 K, respectively. It is noted that the one with F_4TCNQ-doped P3HT shows a much larger coercivity than that with a single Co electrode and the undoped sample. We have two possible deductions regarding this: on one hand, the coercivity of the Co electrode seems to increase as the interfacial roughness of the substrate increases, proved by the atomically-flat surface of silicon oxide wafer and the AFM images of the P3HT layer before and after doping. So, we doubted that the coercivity might be greatly affected by the surface roughness, especially by the uneven F_4TCNQ particles. The surface roughness affects the domain wall movement and causes the increase of coercivity.[53] On the other hand, we suspect that the change of coercivity is more influenced by its spin-dependent hybrid interfacial state. In 2011, Pang *et al.* found that the electrons on the d orbitals of Co atoms will transfer to Alq_3 molecules through the doping effect, leading to a local magnetic moment.[54] Another example is that Co atoms can interact with the O atoms in the Co-doped Alq_3 thin film,

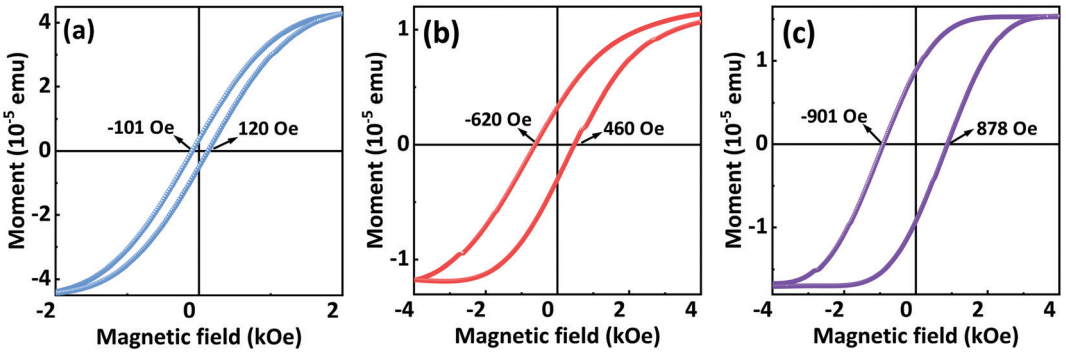

Fig. 5 MR curves of the (a) Co electrode alone, (b) Co electrode with a spin-coated P3HT layer, and (c) Co electrode with a F_4TCNQ-doped P3HT layer.

forming a new state that can act as an electron trap site to localize electrons.[55] Furthermore, as a p-type dopant, F_4TCNQ can accept electrons well, interact with the Co atoms and generate a new hybrid interfacial state to change the coercive force.[56]

3.3. Electrical transport properties

The intrinsic electrical transport analysis of the F_4TCNQ-doped P3HT thin film is beneficial to reveal the interfacial energy barrier and charge transport mechanism. Therefore, the temperature-dependent current–voltage (I–V) tests were carried out. Since the resistance value of the LSMO electrode itself is relatively large which might interfere the evaluation of the natural conductivity of the P3HT thin film, we replaced the previous LSMO electrode with an ITO electrode with similar work function during the measurement. It can be seen from Fig. 6a and b that the IV curves of the devices containing only one FM electrode are non-linear before and after doping, and both curves show a strong temperature dependence, which proves that there is little short circuit caused by the formation of Co metal filaments due to the thermal evaporation process.[30] Meanwhile, when the temperature was reduced from 300 K to 2 K, the resistance value for non-doped and doped P3HT layers increased about 3 times and 90 times, and hence the incomplete Co-penetration induced impurity band and the hopping transport mechanism for charge and spin carriers were deduced, respectively. Besides, the conductivity was significantly enhanced by doping at least one order of magnitude. It is also worth noting that F_4TCNQ doping can effectively modify the interfacial energy barrier, which can be inferred from the opposite rectifying direction in Fig. 6a and b.

The current–temperature (I–T) curves were replotted for the convenience of charge transport mechanism determination. As shown in Fig. 6c and d, both of the curves for non-doped and doped devices exhibited a transition stage for the entire voltage range, except that the doped one showed a significant temperature delay, indicating a change from temperature-dependent thermally activated hopping to a temperature-independent region.[57] As for the thermally activated hopping region, the classical Arrhenius relation was applied to fit the charge transport activation energy E_A,[58] and we obtained average E_A values of 60 meV and 45 meV for the above two thin films. In principle,

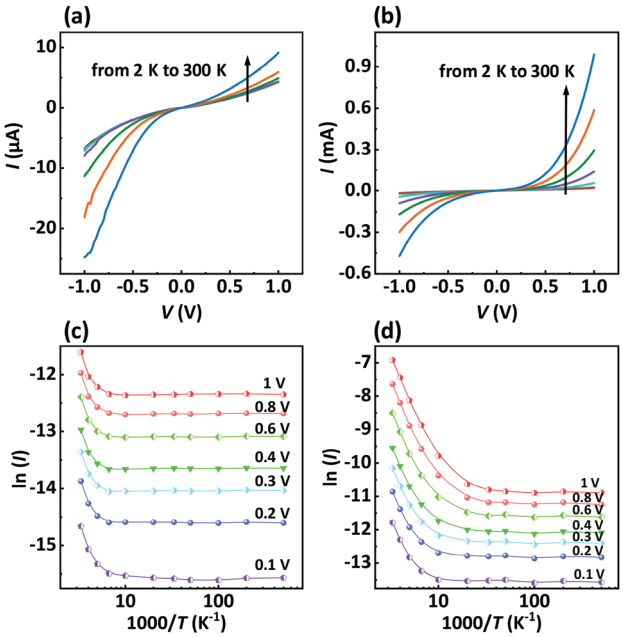

Fig. 6 The temperature-dependent I–V curves of the (a) undoped ITO/P3HT/Co/Au device and (b) doped ITO/P3HT/F_4TCNQ/Co/Au device. The temperature-dependent I–T curves at different voltages of the (c) undoped ITO/P3HT/Co/Au device and (d) doped ITO/P3HT/F_4TCNQ/Co/Au device.

a smaller E_A represents a comparable density of states in P3HT with minor reacted states at the Co/F_4TCNQ interface, leading to a higher conductance. Therefore, it means that the doped-F_4TCNQ could not only effectively modulate the charge injection barrier, but also reversely fill the existing interfacial defects in the P3HT thin film. All the results manifest that interfacial doping of F_4TCNQ is a successful way to optimize electrical transport performance.

3.4. Radical induced spinterface

To further confirm the doping effect of F_4TCNQ at the top interface, we replaced the bottom FM electrode with non-FM ITO for the MR characterization. It can be seen from the MR curves in Fig. 7a that the resistance of the undoped device does not respond to an external magnetic field, while that of the

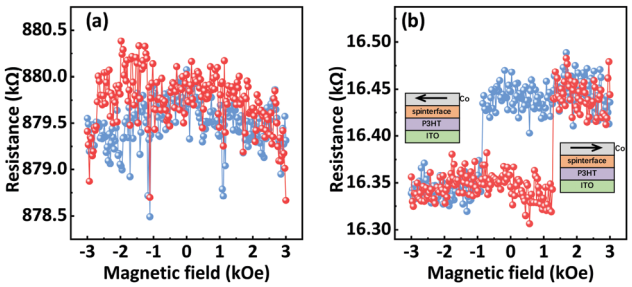

Fig. 7 MR curves of the (a) undoped ITO/P3HT/Co/Au device and (b) doped ITO/P3HT/F_4TCNQ/Co/Au device at T = 2 K, where the input current was 0.01 μA. Insets show the existence of the spinterface (orange box) and magnetization direction of the Co electrode.

doped one shows a regular rectangular shape (Fig. 7b). The triangular background in the ITO/P3HT/Co device is not obvious, which may be caused by the OMAR effect of the P3HT film.[59,60] Fig. S5 and S6 (ESI‡) show the MR curves as a function of input current and temperature, respectively, which verifies the repeatability and authenticity of the rectangular lineshape. More importantly, we found that these switching fields were sensitive to the measurement conditions, for instance, the offset in Fig. S5c (ESI‡) and the shrinking hysteretic window in Fig. S6c and d (ESI‡).

Previous research by Karthik V. Raman *et al.* reported an organic radical induced spinterface, in which the organic layer zinc methyl phenalenyl (ZMP) changed from a neutral to an anionic radical through the charge transfer process and d-orbital hybridization with the interfacial FM electrode.[61] Coincidentally, a rectangular lineshape resembling that in Fig. 7b was observed in the vertical structure of Co/ZMP/Cu with only one FM electrode. Therefore, we speculate that a similar interface magnetoresistance (IMR) effect should be responsible for the MR effect in our case: in the ''half'' spin valve structure, the resistance value changes with the external magnetic field. The high and low resistance states form a loop, which comes from the combination of F_4TCNQ with P3HT in the form of free radicals after doping. Due to the molecular charge transfer, F_4TCNQ is doped into the interface between P3HT and the Co electrode in the form of free radicals, forming a new hybrid interface state. It may produce a resistive spin filter interface, greatly affect the spinterface and induce the related IMR effect.

Unlike traditional OSVs with two FM interfaces that exhibit a standard GMR effect, our F_4TCNQ-doped device not only has a traditional sandwich structure with two FM electrodes, but also includes a spinterface with free radicals after doping. These two mechanisms operate competitively in different devices. Since the hopping transport mechanism of conventional organic spin valves plays a major role in our device, the MR curves are basically well in line with the ''standard'' GMR effect. When the interface states reign, the shape of the curve will change dramatically.[61] Specifically, the absolute value of resistance change in classic OSVs and half OSVs (~20 000 Ω for LSMO/P3HT/F_4TCNQ/Co/Au devices in Fig. 1c and ~100 Ω for ITO/P3HT/F_4TCNQ/Co/Au devices in Fig. 7b) determines the GMR-like dominated lineshape, while the relatively high resistance states or peaks (two repeatable resistance terraces in Fig. 2 and jump points in Fig. 3b and c) in classic OSVs correspond well with the switching field (Fig. S5 and S6, ESI‡) of half OSVs, proving the MR enhancement of the radical-induced spinterface.

4. Conclusions

In conclusion, the F_4TCNQ-doped spinterface plays a key role in improving the spin-dependent signal and conductivity. After doping, the MR ratio of the P3HT-based OSV device increased significantly, and the resistance value declined significantly. The coercivity window of the Co electrode broadened obviously with the existence of a spin-dependent hybrid interfacial state by doping. Through spectral analysis, it was proved that the doping form of F_4TCNQ was a free radical. According to the study of half OSVs, the dopant F_4TCNQ combines with P3HT and Co electrodes formed a spin hybrid state interface, exhibiting a special rectangular MR lineshape. In addition, it is found that when a spinterface is present, the MR response of the F_4TCNQ-doped OSV is influenced by two competitive mechanisms of standard GMR and radical-induced IMR. These results are beneficial for future OSV devices with excellent performance and multistate storage applications.

Conflicts of interest

There are no conflicts to declare.

Acknowledgements

The authors acknowledge the financial support from the National Natural Science Foundation of China (52003190, 21875158, 91833306, 51633006, 51733004) and the National Key R&D Program (2017YFA0204503).

Notes and references

1 G. Binasch, P. Grünberg, F. Saurenbach and W. Zinn, *Phys. Rev. B: Condens. Matter Mater. Phys.*, 1989, **39**, 4828–4830.
2 A. Privitera, M. Righetto, F. Cacialli and M. K. Riede, *Adv. Opt. Mater.*, 2021, **9**, 2100215.
3 Y. Zhao, L. Liu, F. Zhang, C. Di and D. Zhu, *SmartMat*, 2021, 1–20.
4 Z. Ni, H. Wang, H. Dong, Y. Dang, Q. Zhao, X. Zhang and W. Hu, *Nat. Chem.*, 2019, **11**, 271–277.
5 S. M. Duan, X. Gao, Y. Wang, F. X. Yang, M. X. Chen, X. T. Zhang, X. C. Ren and W. P. Hu, *Adv. Mater.*, 2019, **31**, 1807975.
6 Y. Yao, Y. Chen, H. Wang and P. Samorì, *SmartMat*, 2020, **1**, e1009.
7 G. Szulczewski, S. Sanvito and M. Coey, *Nat. Mater.*, 2009, **8**, 693–695.

8 D. Sun, E. Ehrenfreund and Z. V. Vardeny, *Chem. Commun.*, 2014, **50**, 1781–1793.
9 S. Stefano, *Nat. Mater.*, 2007, **6**, 803–804.
10 X. Zhang, J. Tong, H. Zhu, Z. Wang, L. Zhou, S. Wang, T. Miyashita, M. Mitsuishi and G. W. Qin, *J. Mater. Chem. C*, 2017, **5**, 5055–5062.
11 H. Liu, J. Wang, M. Groesbeck, X. Pan, C. Zhang and Z. Vardeny, *J. Mater. Chem. C*, 2018, **6**, 3621–3627.
12 Z. H. Xiong, D. Wu, Z. Valy Vardeny and J. Shi, *Nature*, 2004, **427**, 821–824.
13 V. A. Dediu, L. E. Hueso, I. Bergenti and C. Taliani, *Nat. Mater.*, 2009, **8**, 707–716.
14 T. D. Nguyen, E. Ehrenfreund and Z. V. Vardeny, *Science*, 2012, **337**, 204–209.
15 X. Sun, S. Vélez, A. Atxabal, A. Bedoya-Pinto, S. Parui, X. Zhu, R. Llopis, F. Casanova and L. E. Hueso, *Science*, 2017, **357**, 677–680.
16 L. Guo, X. Gu, X. Zhu and X. Sun, *Adv. Mater.*, 2019, **31**, 1805355.
17 S. Sanvito, *Chem. Soc. Rev.*, 2011, **40**, 3336–3355.
18 J. Devkota, R. Geng, R. C. Subedi and T. D. Nguyen, *Adv. Funct. Mater.*, 2016, **26**, 3881–3898.
19 Y. Zhang, L. Guo, X. Zhu and X. Sun, *Front. Chem.*, 2020, **8**, 589207.
20 D. Li and G. Yu, *Adv. Funct. Mater.*, 2021, **31**, 2100550.
21 S. Schott, U. Chopra, V. Lemaur, A. Melnyk and H. Sirringhaus, *Nat. Phys.*, 2019, **15**, 814–822.
22 L. Guo, Y. Qin, X. Gu, X. Zhu, Q. Zhou and X. Sun, *Front. Chem.*, 2019, **7**, 00428.
23 I. Zutic, J. Fabian and S. D. Sarma, *Rev. Mod. Phys.*, 2004, **76**, 323–410.
24 S. Ding, Y. Tian, X. Liu, Y. Zou, H. Dong, W. Mi and W. Hu, *Nano Res.*, 2021, **14**, 304–310.
25 W. Yang, Q. Shi, T. Miao, Q. Li, P. Cai, H. Liu, H. Lin, Y. Bai, Y. Zhu, Y. Yu, L. Deng, W. Wang, L. Yin, D. Sun, X. G. Zhang and J. Shen, *Nat. Commun.*, 2019, **10**, 3877.
26 S. Ding, Y. Tian and W. Hu, *Nano Res.*, 2021, **14**, 3653–3668.
27 M. F. Sun and W. B. Mi, *J. Mater. Chem. C*, 2018, **6**, 6619–6636.
28 I. Bergenti and V. Dediu, *Nano Mater. Sci.*, 2019, **1**, 149–155.
29 D. Ciudad, M. Gobbi, C. J. Kinane, M. Eich, J. S. Moodera and L. E. Hueso, *Adv. Mater.*, 2014, **26**, 7561–7567.
30 S. Ding, Y. Tian, Y. Li, W. Mi, H. Dong, X. Zhang, W. Hu and D. Zhu, *ACS Appl. Mater. Interfaces*, 2017, **9**, 15644–15651.
31 C. Barraud, P. Seneor, R. Mattana, S. Fusil, K. Bouzehouane, C. Deranlot, P. Graziosi, L. Hueso, I. Bergenti, V. Dediu, F. Petroff and A. Fert, *Nat. Phys.*, 2010, **6**, 615–620.
32 M. Galbiati, S. Tatay, C. Barraud, A. V. Dediu, F. Petroff, R. Mattana and P. Seneor, *MRS Bull.*, 2014, **39**, 602–607.
33 M. Cinchetti, V. A. Dediu and L. E. Hueso, *Nat. Mater.*, 2017, **16**, 507–515.
34 Y. Yamashita, J. Tsurumi, M. Ohno, R. Fujimoto, S. Kumagai, T. Kurosawa, T. Okamoto, J. Takeya and S. Watanabe, *Nature*, 2019, **572**, 634–638.
35 M. Schwarze, C. Gaul, R. Scholz, F. Bussolotti, A. Hofacker, K. S. Schellhammer, B. Nell, B. D. Naab, Z. Bao, D. Spoltore, K. Vandewal, J. Widmer, S. Kera, N. Ueno, F. Ortmann and K. Leo, *Nat. Mater.*, 2019, **18**, 242–248.
36 S.-J. Wang, D. Venkateshvaran, M. R. Mahani, U. Chopra, E. R. McNellis, R. Di Pietro, S. Schott, A. Wittmann, G. Schweicher, M. Cubukcu, K. Kang, R. Carey, T. J. Wagner, J. N. M. Siebrecht, D. P. G. H. Wong, I. E. Jacobs, R. O. Aboljadayel, A. Ionescu, S. A. Egorov, S. Mueller, O. Zadvorna, P. Skalski, C. Jellett, M. Little, A. Marks, I. McCulloch, J. Wunderlich, J. Sinova and H. Sirringhaus, *Nat. Electron.*, 2019, **2**, 98–107.
37 A. Privitera, R. Warren, G. Londi, P. Kaienburg and M. Riede, *J. Mater. Chem. C*, 2021, **9**, 2944–2954.
38 S. Delprat, M. Galbiati, S. Tatay, B. Quinard, C. Barraud, F. Petroff, P. Seneor and R. Mattana, *J. Phys. D: Appl. Phys.*, 2018, **51**, 473001.
39 D. T. Scholes, S. A. Hawks, P. Y. Yee, H. Wu, J. R. Lindemuth, S. H. Tolbert and B. J. Schwartz, *J. Phys. Chem. Lett.*, 2015, **6**, 4786–4793.
40 S. Ding, Y. Tian, H. Wang, Z. Zhou, W. Mi, Z. Ni, Y. Zou, H. Dong, H. Gao, D. Zhu and W. Hu, *ACS Nano*, 2018, **12**, 12657–12664.
41 B. Maennig, M. Pfeiffer, A. Nollau, X. Zhou, K. Leo and P. Simon, *Phys. Rev. B: Condens. Matter Mater. Phys.*, 2001, **64**, 195208.
42 A. Hamidi-Sakr, L. Biniek, J. L. Bantignies, D. Maurin, L. Herrmann, N. Leclerc, P. Leveque, V. Vijayakumar, N. Zimmermann and M. Brinkmann, *Adv. Funct. Mater.*, 2017, **27**, 1700173.
43 P. Pingel and D. Neher, *Phys. Rev. B: Condens. Matter Mater. Phys.*, 2013, **87**, 115209.
44 H.-J. Jang and C. A. Richter, *Adv. Mater.*, 2017, **29**, 1602739.
45 W. Sun, L. Guo, S. Hu, X. Zhu, X. Zhang, W. Hu and X. Sun, *Org. Electron.*, 2021, **99**, 106311.
46 M. Wohlgenannt, *Phys. Status Solidi RRL*, 2012, **6**, 229–242.
47 X. Sun, A. Bedoya-Pinto, Z. Mao, M. Gobbi, W. Yan, Y. Guo, A. Atxabal, R. Llopis, G. Yu, Y. Liu, A. Chuvilin, F. Casanova and L. E. Hueso, *Adv. Mater.*, 2016, **28**, 2609–2615.
48 W. R. Zhao, J. M. Ding, Y. Zou, C. A. Di and D. B. Zhu, *Chem. Soc. Rev.*, 2020, **49**, 7210–7228.
49 S. N. Patel, A. M. Glaudell, K. A. Peterson, E. M. Thomas, K. A. O'Hara, E. Lim and M. L. Chabinyc, *Sci. Adv.*, 2017, **3**, e1700434.
50 H. Méndez, G. Heimel, S. Winkler, J. Frisch, A. Opitz, K. Sauer, B. Wegner, M. Oehzelt, C. Röthel, S. Duhm, D. Többens, N. Koch and I. Salzmann, *Nat. Commun.*, 2015, **6**, 8560.
51 D. T. Scholes, P. Y. Yee, J. R. Lindemuth, H. Kang, J. Onorato, R. Ghosh, C. K. Luscombe, F. C. Spano, S. H. Tolbert and B. J. Schwartz, *Adv. Funct. Mater.*, 2017, **27**, 1702654.
52 I. E. Jacobs and A. Moulé, *Adv. Mater.*, 2017, **29**, 1703063.
53 Y.-P. Zhao, R. M. Gamache, G.-C. Wang, T.-M. Lu, G. Palasantzas and J. T. M. D. Hosson, *J. Appl. Phys.*, 2001, **89**, 1325–1330.
54 Z. Y. Pang, L. Lin, F. G. Wang, S. J. Fang, Y. Dai and S. H. Han, *Appl. Phys. Lett.*, 2011, **99**, 153306.

55 J. M. Baik, Y. Shon, S. J. Lee, Y. H. Jeong, T. W. Kang and J.-L. Lee, *J. Am. Chem. Soc.*, 2008, **130**, 13522–13523.
56 Y. Hsu, Y. Lai, C. Chen, Y. Lin, H. Chien, J. Wang, T. Lam, Y. Chan, D. H. Wei, H. Lin and C. Chen, *J. Phys. Chem. Lett.*, 2013, **4**, 310–316.
57 C. C. Bof Bufon, C. Vervacke, D. J. Thurmer, M. Fronk, G. Salvan, S. Lindner, M. Knupfer, D. R. T. Zahn and O. G. Schmidt, *J. Phys. Chem. C*, 2014, **118**, 7272–7279.
58 R. L. McCreery, *Chem. Mater.*, 2004, **16**, 4477–4496.
59 R. Geng, R. C. Subedi, H. M. Luong, M. T. Pham and T. D. Nguyen, *Phys. Rev. Lett.*, 2018, **120**, 086602.
60 Ö. Mermer, G. Veeraraghavan, T. L. Francis, Y. Sheng, D. T. Nguyen, M. Wohlgenannt, A. Köhler, M. K. Al-Suti and M. S. Khan, *Phys. Rev. B: Condens. Matter Mater. Phys.*, 2005, **72**, 205202.
61 K. V. Raman, A. M. Kamerbeek, A. Mukherjee, N. Atodiresei, T. K. Sen, P. Lazić, V. Caciuc, R. Michel, D. Stalke, S. K. Mandal, S. Blügel, M. Münzenberg and J. S. Moodera, *Nature*, 2013, **493**, 509–513.